Nonequilibrium currents in stochastic field theories: A geometric insight

J. O'Byrne

Université Paris-Cité, Laboratoire Matière et Systèmes Complexes (MSC), UMR 7057 CNRS, F-75205 Paris, France and DAMTP, University of Cambridge, Wilberforce Road, Cambridge CB3 0WA, United Kingdom

(Received 19 January 2023; accepted 3 April 2023; published 2 May 2023)

We introduce a formalism to study nonequilibrium steady-state probability currents in stochastic field theories. We show that generalizing the exterior derivative to functional spaces allows identification of the subspaces in which the system undergoes local rotations. In turn, this allows prediction of the counterparts in the real, physical space of these abstract probability currents. The results are presented for the case of the Active Model B undergoing motility-induced phase separation, which is known to be out of equilibrium but whose steady-state currents have not yet been observed, as well as for the Kardar-Parisi-Zhang equation. We locate and measure these currents and show that they manifest in real space as propagating modes localized in regions with nonvanishing gradients of the fields.

DOI: 10.1103/PhysRevE.107.054105

I. INTRODUCTION

Statistical physics aims to describe large-scale phenomena emerging from interacting elementary constituents, ranging from chemicals to animals, and from bacteria to traders. Except when systems satisfy a detailed balance, no general theory can be systematically applied to study such systems. To understand how microscopic mechanisms drive a system out of equilibrium, physicists have been quantifying the distance to equilibrium using diverse observables, such as the entropy production [1–5], violations of the fluctuation-dissipation theorem [6,7], or ratchet currents [8–11]. Among those, the stationary probability current plays an important role since its knowledge, together with the stationary probability measure, entirely determine the equations of motion (see [12–14] and Sec. II). For systems driven out of equilibrium by external fields [15–17] or boundary conditions [18,19], probability currents directly lead to real-space currents—e.g., of energy or mass—that can be observed and quantified easily. In many other situations, as in active systems [20–25], surface growth problems [26], or reaction-diffusion processes [27], probability currents live in high-dimensional configuration spaces and have no simple low-dimensional projection in real space, which makes their study challenging.

While probability currents are well understood for finite-dimensional systems [28–38], collective behaviors are best described at a macroscopic scale using field theory [39–41]. The nonequilibrium nature of such infinite-dimensional description has attracted a lot of interest recently [15,21,42–44], but the identification of their *probability* currents remains elusive. Progress has been made in specific situations [45,46], but a generic framework is crucially lacking.

In this article, we address this challenge by introducing a mathematical framework that enables a systematic characterization of steady-state probability currents in nonequilibrium stochastic field theories. This framework is based on a generalization of the curl operator to functional spaces in the form of a functional exterior derivative and on the identification of the appropriate Riemannian metric on the space of fields. We note that a related object, called "vertical derivative," has been introduced for jet bundles [47], a context more restrictive than what we present here—since it cannot handle nonlocal functionals, for instance. In addition, differential geometry has been formally extended to abstract mathematical spaces [48], but the corresponding level of abstraction makes such theory hardly applicable to concrete physics problems. Furthermore, these mathematical formalisms have never been applied to characterize probability currents in stochastic field theories. Below, we briefly recap the finite-dimensional case to highlight the key steps of its generalization to infinite dimension. We then detail the construction of the functional exterior derivative for two important examples: the Active Model B (AMB) [49] and the Kardar-Parisi-Zhang (KPZ) equation [26]. Importantly, when undergoing motility-induced phase separation (MIPS), AMB leads to a finite entropy production rate localized at the liquid-gas interface [21,50]. However, the corresponding probability currents have remained out of reach so far. Here, we show how these currents can be decomposed into superpositions of local two-dimensional (2D) rotations, allowing for direct observation (see Fig. 1). Our framework also reveals the direct manifestations of these high-dimensional currents in real space, in the form of propagating modes localized at the liquid-gas interface (see Fig. 2). Similarly, for the KPZ equation, we show how fluctuations are advected along height gradients (see Fig. 4).

II. REMINDER OF THE FINITE–DIMENSIONAL CASE

To set the stage for stochastic field theories, we start with a quick reminder of the well-known finite-dimensional case. Consider the n-dimensional Langevin dynamics,

$$\dot{\mathbf{r}}(t) = \mathbf{F}(\mathbf{r}(t)) + \sqrt{2D}\boldsymbol{\eta}(t), \tag{1}$$

where $\mathbf{r}(t) \in \mathbb{R}^n$, $\boldsymbol{\eta}$ is a Gaussian white noise of zero mean and unit variance, D is the diffusion constant, the mobility has

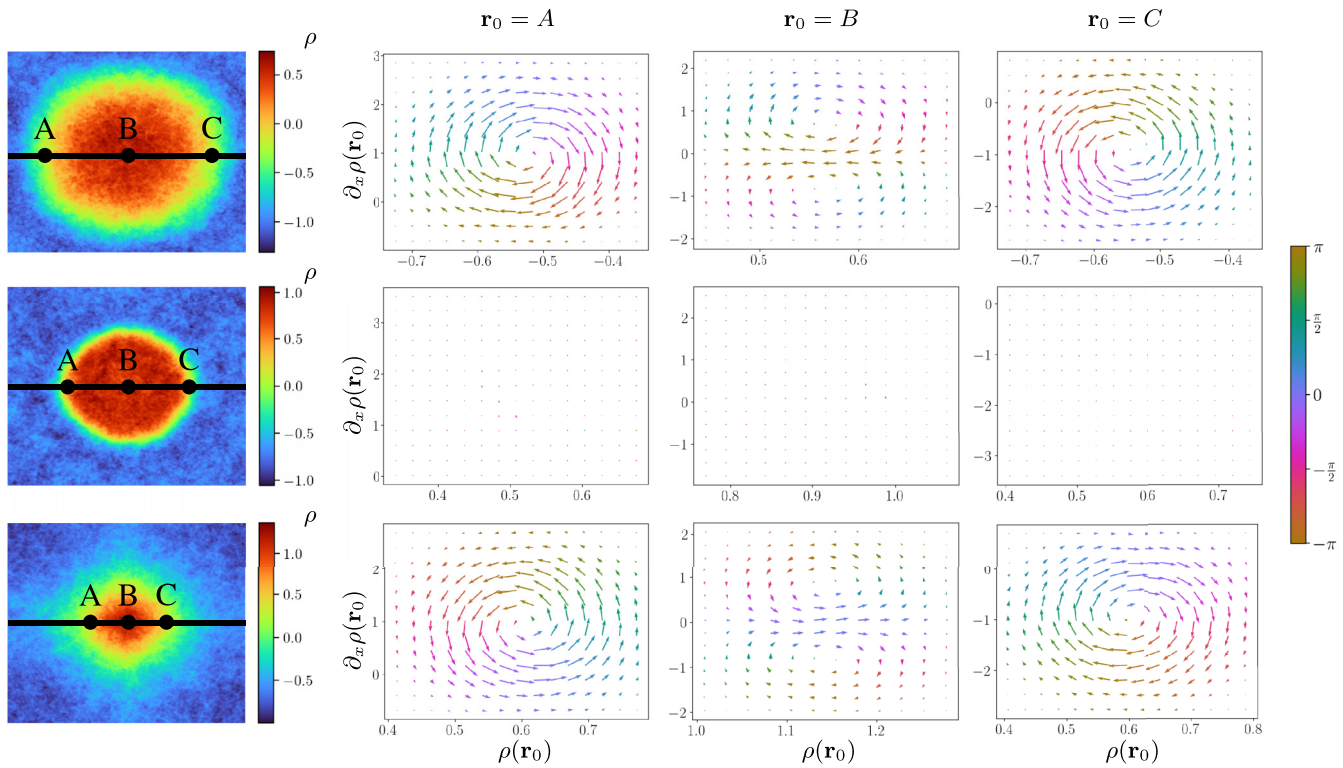

FIG. 1. Measurements of the stationary probability currents in the planes $[\rho(\mathbf{r}_0), \partial_x \rho(\mathbf{r}_0)]$ at representative points in phase-separated systems, using numerical resolution of Eq. (9). The rows correspond to $2\lambda + \kappa' < 0$ (top), $2\lambda + \kappa' = 0$ (center), and $2\lambda + \kappa' > 0$ (bottom), respectively. The average stationary profiles are shown in the left column. Other columns show the current vector fields measured at the corresponding points $\mathbf{r}_0 = A, B, C$ in the phase-separated profiles. (Arrow colors encode their angles with respect to $\mathbf{e}_x$.) Parameters: $a = -1$, $b = 1$, $\kappa = 0.1$, average density $\rho_0 = -0.4$, $D = 10^{-3}$, $L_x = L_y = 10$, and $\lambda = -2$ (top), 0 (center), and 2 (bottom). See Appendices A and B for numerical details.

been set to 1, and $\mathbf{F}$ is an arbitrary smooth vector field. The corresponding Fokker-Planck equation reads

$$\partial_t p = -\nabla \cdot \mathbf{J} \quad \text{with} \quad \mathbf{J} = p\mathbf{F} - D\nabla p. \tag{2}$$

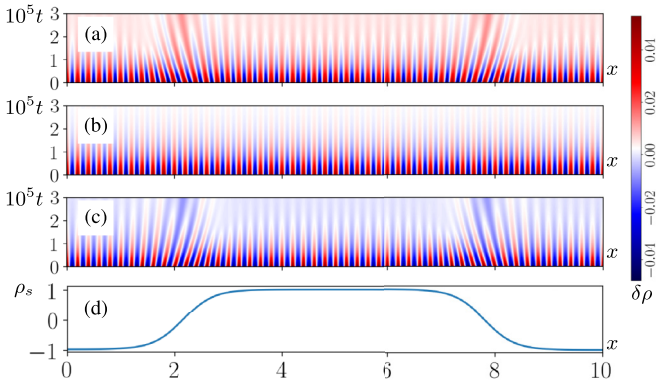

FIG. 2. Evolution of a perturbation $\delta\rho$ around the equilibrium profile ρ_s under the AMB dynamics (9) using periodic boundary conditions and $\delta\rho(x, y, t = 0) = \varepsilon \cos(100\pi x/L_x)$. (a)–(c) Kymographs representing the evolution of $\delta\rho(x, L_y/2, t)$. (d) A cut of ρ_s at $y = L_y/2$. Parameters: $\rho_0 = -0.45$, $a = -1$, $b = 1$, $\kappa = 0.15$, $dt = 10^{-7}$, $dx = dy = 10^{-2}$, $L_x = L_y = 10$, $\varepsilon = 0.05$, and $\lambda = -4$, 0, and 4 for (a)–(c), respectively. Time axis unit of the kymographs is $\Delta t = 10^{-5}$.

Note that as stated in Sec. I, the joint knowledge of the stationary probability density p_s and current $\mathbf{J}_s$ (together with D) entirely determines Eq. (1) since $\mathbf{F} = \mathbf{J}_s/p_s + D\nabla \ln p_s$.

Importantly, the stationary probability current $\mathbf{J}_s$ encodes the advection of the probability p_s by the mean velocity field,

$$\mathbf{v}_s \equiv \mathbf{J}_s/p_s = \mathbf{F} - D\nabla \ln p_s. \tag{3}$$

The flow lines of $\mathbf{v}_s$ indicate the typical trajectories of the system in the steady state [14]. Because it favors certain trajectories over their time-reversed counterparts, the swirling behavior of $\mathbf{v}_s$ is responsible for the irreversibility of dynamics (1). When $n = 3$, it is characterized by the vorticity

$$\boldsymbol{\omega}(\mathbf{r}) \equiv \nabla \times \mathbf{v}_s(\mathbf{r}) = \nabla \times \mathbf{F}(\mathbf{r}), \tag{4}$$

whose norm gives the angular speed of the local swirls, and whose direction is orthogonal to the local two-dimensional planes in which the current undergoes local rotations. Further, note that the entropy production rate of dynamics (1) is given by [5]

$$\sigma = \frac{1}{D} \int \mathbf{J}_s(\mathbf{r}) \cdot \mathbf{F}(\mathbf{r}) d\mathbf{r}. \tag{5}$$

Since $\mathbf{J}_s$ is divergence free and $\mathbb{R}^n$ simply connected, there is a vector field $\mathbf{C}$ such that $\mathbf{J}_s = \nabla \times \mathbf{C}$. Injecting this last

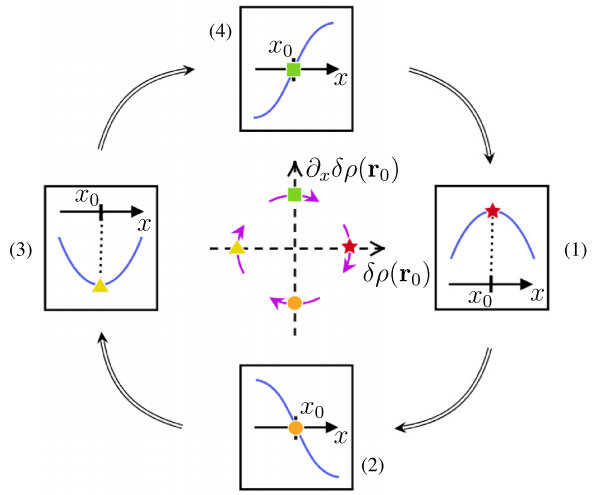

FIG. 3. Analysis of the currents shown in Fig. 1 predicting the mode propagation reported in Fig. 2. Consider the case $2\lambda + \kappa' < 0$ and a point $\mathbf{r}_0 = (x_0, L_y/2)$ on the left boundary of the droplet (top row, column *A* of Fig. 1). In the central panel, we show the circulation induced by the current in the $[\delta\rho(\mathbf{r}_0), \partial_x\delta\rho(\mathbf{r}_0)]$ plane. Consider a perturbation such that $\delta\rho(\mathbf{r}_0)$ is a local maximum at $t = 0$ [panel (1), red star]. As time goes on, the current drives the fluctuation sequentially from (1) to (2) (orange dot), to (3) (yellow triangle), and to (4) (green square). Each panel shows the fluctuation profile $\delta\rho(x, L_y/2)$ around x_0 (blue curves). These successive states of $\delta\rho$ show that the probability current corresponds to a leftward propagation of $\delta\rho$ in the real space, from the liquid to the gas phase. Inspection of Fig. 1 allows prediction of all the dynamics reported in Fig. 2.

equality into Eq. (5) and integrating by parts leads to

$$\sigma = \frac{1}{D}\int \mathbf{C}(\mathbf{r})\cdot\boldsymbol{\omega}(\mathbf{r})d\mathbf{r}. \tag{6}$$

Hence, $\boldsymbol{\omega}(\mathbf{r})$ can be seen as the local source of entropy production and $\mathbf{C}(\mathbf{r})$ as a weight over the infinitesimal loops around $\mathbf{r}$. In fact, $D^{-1}\boldsymbol{\omega}$ and C have recently been identified as the continuous-space analogs of cycle affinity and flux [51], respectively, quantities that turn out to be crucial to characterize the irreversibility of Markov chains [52,53].

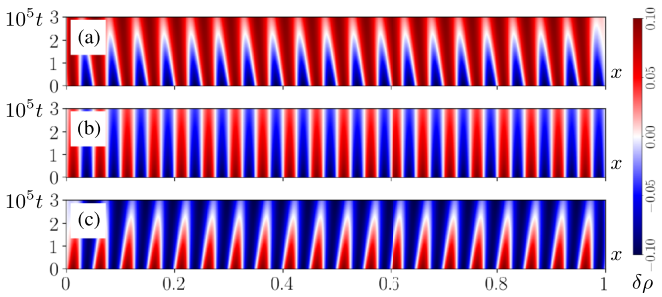

FIG. 4. Kymographs showing the zero-noise relaxation of a perturbation $\delta h(x) = 0.1\sin(40\pi x)$, added at time $t = 0$ to a linear profile $h(x) = 10x$, under the KPZ dynamics (43) with Dirichlet boundary conditions. Parameters: $\nu = 2$ and $\lambda = -16, 0, 16$ for (a)–(c), respectively. System size $L = 1$. Space and time discretization: $dx = 10^{-3}$ and $dt = 10^{-7}$.

The generalization to arbitrary but finite dimension n amounts to replacing $\nabla\times\mathbf{F}$ by $d\mathbf{F}^\flat$ in the vorticity $\boldsymbol{\omega}$, where d is the exterior derivative and $\mathbf{F}^\flat$ the one-form associated to $\mathbf{F}$ through a Riemannian metric g [54]. Denote by $(\mathbf{e}_i)_{i=1,\dots,d}$ a local basis and $(dx^i)_{i=1,\dots,d}$ its dual, which satisfies $dx^i(\mathbf{e}_j) = \delta^i_j$. Then, to $\mathbf{F} = \sum_i F^i\mathbf{e}_i$, we associate the one-form $\mathbf{F}^\flat = \sum_i F_i dx^i = \sum_{i,j} g_{ij}F^j dx^i$ with $g_{ij} \equiv g(\mathbf{e}_i, \mathbf{e}_j)$. The exterior derivative of $\mathbf{F}^\flat$ is then the two-form $\mathrm{d}\mathbf{F}^\flat$, whose action on arbitrary pairs $\mathbf{u}$, $\mathbf{v}$ of vector fields reads

$$d\mathbf{F}^\flat(\mathbf{u},\mathbf{v}) = \sum_{i,j=1}^{n}\left(\frac{\partial F_j}{\partial x_i} - \frac{\partial F_i}{\partial x_j}\right)u^i v^j. \tag{7}$$

Denoting by $dx^i\wedge dx^j$ the bilinear maps such that $dx^i\wedge dx^j(\mathbf{u},\mathbf{v}) = u^iv^j - u^jv^i$, the vorticity reads

$$\boldsymbol{\omega} \equiv d\mathbf{F}^\flat = \sum_{1\leqslant i<j\leqslant n}\left(\frac{\partial F_j}{\partial x_i} - \frac{\partial F_i}{\partial x_j}\right)dx^i\wedge dx^j. \tag{8}$$

The prefactor of $dx^i\wedge dx^j$ in Eq. (8) measures the local rotation induced by $\mathbf{F}$ in the $(\mathbf{e}_i, \mathbf{e}_j)$ plane: its sign gives the direction of the rotation and its amplitude the angular speed. Finally, note that dynamics (1) is reversible if and only if $d\mathbf{F}^\flat = 0$. Then, $\mathbf{F}$ is a gradient and Eq. (1) is a stochastic gradient descent.

III. NONEQUILIBRIUM FIELD THEORIES

We now turn to the core results of this article: the generalization of Eq. (8) to infinite-dimensional stochastic field theory and the physical insight it provides on the corresponding systems. For an arbitrary field theory, this requires generalizing the $\flat$ and d operators. The former amounts to finding the Riemannian metric that identifies a reversible dynamics with a gradient descent of the free energy; it also associates a one-form to the deterministic drift. The exterior derivative then extracts the skew-symmetric part of the corresponding Jacobian, which vanishes for equilibrium dynamics and identifies the nonequilibrium circulations otherwise. These ideas can be applied to any overdamped, Gaussian, stochastic field dynamics. In this article, for the sake of clarity, we present them on two important examples, i.e., the AMB and the KPZ equation.

A. Active Model B

We start with the study of AMB, which has attracted a lot of interest recently [21,49], and whose probability currents have remained elusive so far. AMB describes a scalar field whose dynamics is given by

$$\partial_t\rho = -\nabla\cdot\mathbf{j} \quad\text{with}\quad \mathbf{j} = -\nabla\mu + \sqrt{2D}\boldsymbol{\Lambda}. \tag{9}$$

In Eq. (9), $\boldsymbol{\Lambda}(\mathbf{r},t)$ is a centered Gaussian white noise field of unit variance and μ a nonequilibrium chemical potential defined by

$$\mu([\rho],\mathbf{r}) = a\rho + b\rho^3 - \kappa(\rho)\Delta\rho + \lambda(\rho)|\nabla\rho|^2. \tag{10}$$

Note that a, b, and D are constants, but λ and κ depend on $\rho(\mathbf{r})$.

Comparing (9) to the finite-dimensional dynamics (1), we see that the configuration of the system, which was given by

the vector $\mathbf{r} \in \mathbb{R}^d$ in Eq. (1), is now replaced by the density field ρ. We denote by $\mathbb{F}$ the functional space to which the field ρ belongs.

In order to generalize (8), we first identify, in Sec. III A 1, the appropriate notions of vector fields and one-forms on $\mathbb{F}$. In Sec. III A 2, we determine the suitable Riemannian metric that allows interpretation of a reversible dynamics as a stochastic gradient descent of the free energy. In addition, this Riemannian metric induces a mapping between functional one-forms and vector fields that we exploit thereafter. We then turn to generalizing the exterior derivative to the functional space $\mathbb{F}$ in Sec. III A 4 and use this operator to define a functional vorticity analogous to Eq. (8). In Sec. III A 5, we carry out the explicit computation of the vorticity of AMB. Finally, we show in Sec. III A 6 that this functional vorticity allows identification of the structure of the probability currents in $\mathbb{F}$, as well as their counterpart in the physical space in the form of anisotropic propagating modes localized at the liquid-gas interface of a phase-separated profile.

1. Functional one-forms and vector fields

First, we restrict $\mathbb{F}$ to fields satisfying all the integrability and regularity conditions so that our manipulations are valid. Then we note that the total number of particles is conserved by dynamics (9). Thus, a small variation $\delta\rho(\mathbf{r})$ of a given $\rho \in \mathbb{F}$—i.e., a tangent vector at ρ—should preserve this constraint and hence integrate to zero over the whole space. In turn, a vector field over $\mathbb{F}$ is a scalar-valued functional of ρ and a function of $\mathbf{r}$ that integrates to zero with respect to $\mathbf{r}$, for any $\rho \in \mathbb{F}$. We denote such function(al) as $\boldsymbol{\mu}(\mathbf{r}, [\rho])$ in boldface, with the reason for this notation justified in what follows.

We further note that since the divergence operator is a surjective map from real-space vector fields to functions whose integral vanishes, for any $\boldsymbol{\mu}$ there exists a mass current $\mathbf{j}(\mathbf{r}, [\rho])$ such that $\boldsymbol{\mu} = -\nabla \cdot \mathbf{j}$. In addition, $\mathbf{j}(\cdot, [\rho])$ can always be decomposed as the superposition of a gradient and a divergence-free vector field. The divergence of the latter being zero, it vanishes in the relation between $\boldsymbol{\mu}$ and $\mathbf{j}$. We thus get that for any functional vector field $\boldsymbol{\mu}$, there exists a scalar function(al) $\mu(\mathbf{r}, [\rho])$, called the chemical potential associated to $\boldsymbol{\mu}$, such that

$$\boldsymbol{\mu}(\mathbf{r}, [\rho]) \equiv -\Delta\mu(\mathbf{r}, [\rho]). \tag{11}$$

We finally identify chemical potentials $\mu(\mathbf{r}, [\rho])$ that only differ by a harmonic function so that Eq. (11) can be seen as a one-to-one mapping between chemical potentials μ and functional vector fields $\boldsymbol{\mu}$.

We now turn to functional one-forms over $\mathbb{F}$. A functional one-form α associates to any $\rho \in \mathbb{F}$ a linear function that maps a tangent vector $\boldsymbol{\mu}(\cdot, [\rho])$ at ρ to a real number. As such, it can be written as

$$\alpha(\boldsymbol{\mu})|_\rho = \int \alpha(\mathbf{r}, [\rho])\boldsymbol{\mu}(\mathbf{r}, [\rho])d\mathbf{r}, \tag{12}$$

where $\alpha(\mathbf{r}, [\rho])$ is a functional of ρ and a (possibly generalized) function of $\mathbf{r}$—that is temporarily denoted by the same letter as the associated one-form. Note that for a given one-form α, the function(al) $\alpha(\mathbf{r}, [\rho])$ is not unique. Indeed, since any vector field reads $\boldsymbol{\mu} = -\Delta\mu$, integrating by parts in Eq. (12) shows $\alpha(\mathbf{r}, [\rho])$ to be defined up to any $h(\mathbf{r}, [\rho])$ that is harmonic with respect to $\mathbf{r}$. In other words, just as functional vector fields, functional one-forms are in one-to-one correspondence with chemical potentials. Consequently, for any chemical potential $\mu_0(\mathbf{r}, [\rho])$, we will denote the associated one-form as α_{μ_0}, i.e.,

$$\alpha_{\mu_0}(\boldsymbol{\mu}) = \int \mu_0(\mathbf{r}, [\rho])\boldsymbol{\mu}(\mathbf{r}, [\rho])d\mathbf{r}. \tag{13}$$

2. Riemannian metric

First, note that the functional Fokker-Planck equation associated to (9) reads

$$\partial_t P[\rho] = -\int d\mathbf{r}\, \frac{\delta\, \mathbf{J}(\mathbf{r}, [\rho])}{\delta\rho(\mathbf{r})}, \tag{14}$$

where $\mathbf{J}$ is the probability current given by

$$\mathbf{J}(\mathbf{r}, [\rho]) = P[\rho]\Delta\mu(\mathbf{r}, [\rho]) + D\Delta\frac{\delta P[\rho]}{\delta\rho(\mathbf{r})}. \tag{15}$$

Equation (9) is reversible if and only if the stationary probability current $\mathbf{J}_s$ vanishes. Using that $\boldsymbol{\mu} = -\Delta\mu$, this conditions reads $\boldsymbol{\mu} = DP_s[\rho]^{-1}\Delta\frac{\delta P_s[\rho]}{\delta\rho(\mathbf{r})}$, which turns out to be equivalent to the existence of a functional $\mathcal{F}$ such that

$$\boldsymbol{\mu} = -\Delta\frac{\delta\mathcal{F}}{\delta\rho}. \tag{16}$$

Then, our choice of metric is constrained by the requirement that Eq. (16) has to be equivalent to $\boldsymbol{\mu}$ being the gradient of $\mathcal{F}$. This is the infinite-dimensional analog to $-F^i = (\nabla V)^i$ and reads

$$\boldsymbol{\mu} = \mathbf{grad}\,\mathcal{F} = -\Delta\frac{\delta\mathcal{F}}{\delta\rho}. \tag{17}$$

Let us now show how this determines the metric g, which we write as

$$g(\boldsymbol{\mu}_1, \boldsymbol{\mu}_2) = \int \boldsymbol{\mu}_1(\mathbf{r}, [\rho])\mathbf{G}(\mathbf{r}, \mathbf{r}')\boldsymbol{\mu}_2(\mathbf{r}', [\rho])\, d\mathbf{r}\, d\mathbf{r}', \tag{18}$$

where $\mathbf{G}$ is a symmetric positive kernel.

We start from the general definition of a gradient,

$$\forall\boldsymbol{\mu}_0, \quad g(\mathbf{grad}\mathcal{F}, \boldsymbol{\mu}_0) \equiv \delta\mathcal{F}(\boldsymbol{\mu}_0), \tag{19}$$

where $\delta\mathcal{F}$ is the differential of $\mathcal{F}[\rho]$, given by

$$\delta\mathcal{F}(\boldsymbol{\mu}_0) \equiv \int \frac{\delta\mathcal{F}[\rho]}{\delta\rho(\mathbf{r})}\boldsymbol{\mu}_0(\mathbf{r}, [\rho])d\mathbf{r}. \tag{20}$$

Using Eqs. (18) and (20), Eq. (19) can be rewritten as

$$\int \mathbf{grad}\mathcal{F}(\mathbf{r}, [\rho])\, \mathbf{G}(\mathbf{r}, \mathbf{r}')\boldsymbol{\mu}_0(\mathbf{r}', [\rho])d\mathbf{r}d\mathbf{r}' = \int \frac{\delta\mathcal{F}[\rho]}{\delta\rho(\mathbf{r})}\boldsymbol{\mu}_0(\mathbf{r}, [\rho])d\mathbf{r}. \tag{21}$$

The constraint (17) then leads to

$$\int -\Delta_{\mathbf{r}}\frac{\delta\mathcal{F}[\rho]}{\delta\rho(\mathbf{r})}\mathbf{G}(\mathbf{r}, \mathbf{r}')\boldsymbol{\mu}_0(\mathbf{r}', [\rho])d\mathbf{r}d\mathbf{r}' = \int \frac{\delta\mathcal{F}[\rho]}{\delta\rho(\mathbf{r})}\boldsymbol{\mu}_0(\mathbf{r}, [\rho])d\mathbf{r}. \tag{22}$$

Performing an integration by parts on this last equation gives

$$\int -\frac{\delta\mathcal{F}[\rho]}{\delta\rho(\mathbf{r})}\Delta_{\mathbf{r}}\mathbf{G}(\mathbf{r},\mathbf{r}')\boldsymbol{\mu}_0(\mathbf{r}',[\rho])d\mathbf{r}d\mathbf{r}' = \int \frac{\delta\mathcal{F}[\rho]}{\delta\rho(\mathbf{r})}\boldsymbol{\mu}_0(\mathbf{r},[\rho])d\mathbf{r}. \tag{23}$$

Since this last equality is required for any functional $\mathcal{F}$ and any functional vector field $\boldsymbol{\mu}_0$, we conclude that

$$\mathbf{G}(\mathbf{r},\mathbf{r}') = -\Delta_{\mathbf{r}}^{-1}\delta(\mathbf{r}-\mathbf{r}'). \tag{24}$$

For any pair of functional vector fields $\boldsymbol{\mu}_1 = -\Delta\mu_1$, $\boldsymbol{\mu}_2 = -\Delta\mu_2$, inserting Eq. (24) into Eq. (18) finally leads, after integrating by parts, to the Riemannian metric,

$$g(\boldsymbol{\mu}_1,\boldsymbol{\mu}_2) = \int \nabla\mu_1\cdot\nabla\mu_2 d\mathbf{r}. \tag{25}$$

Note that the noise of the Active Model B is additive. But if it were multiplicative with an amplitude proportional to $\sqrt{\rho}$—as is the case when the stochastic hydrodynamics is explicitly derived from a set of microscopic stochastic equations with additive noise (see, e.g., [55])—then the corresponding Riemannian metric would be the Otto metric and hence would induce the Wasserstein distance on $\mathbb{F}$ [56].

3. From functional vector fields to one-forms

As in finite dimension, the Riemannian metric (25) allows one to map any vector field $\boldsymbol{\mu}_1$ to a (functional) one-form, denoted by $\boldsymbol{\mu}_1^\flat$, through

$$\boldsymbol{\mu}_1^\flat(\cdot) \equiv g(\boldsymbol{\mu}_1,\cdot). \tag{26}$$

Performing an integration by parts in equation Eq. (26) leads to the relation

$$\boldsymbol{\mu}_1^\flat(\boldsymbol{\mu}_2) = \int \mu_1(\mathbf{r},[\rho])\boldsymbol{\mu}_2(\mathbf{r},[\rho])d\mathbf{r}, \tag{27}$$

where $\boldsymbol{\mu}_2$ is an arbitrary vector field. Hence, applying the one-form $\boldsymbol{\mu}_1^\flat$ to any vector field $\boldsymbol{\mu}_2$ at $\rho\in\mathbb{F}$ amounts to integrating $\boldsymbol{\mu}_2(\mathbf{r},[\rho])$ against the chemical potential $\mu_1(\mathbf{r},[\rho])$ associated to $\boldsymbol{\mu}_1$ through (11). First, this means that $\boldsymbol{\mu}_1^\flat = \alpha_{\mu_1}$, as defined in (13). Furthermore, $\mu_1(\mathbf{r},[\rho])$ plays, for the one-form $\boldsymbol{\mu}_1^\flat$, a role similar to the one played by the (covariant) coordinates $F_i(\mathbf{r})$ for $\mathbf{F}^\flat$ in finite dimension. This last point will turn out to be crucial for generalizing the exterior derivative to functional space in the next section.

4. The functional exterior derivative

We now turn to the construction of the functional exterior derivative. Inspired by the finite-dimensional case given by Eq. (7), we define the functional exterior derivative of a one-form $\boldsymbol{\mu}^\flat$ through its action on an arbitrary pair $(\boldsymbol{\phi},\boldsymbol{\psi})$ of vector fields as

$$\mathbb{d}\boldsymbol{\mu}^\flat(\boldsymbol{\phi},\boldsymbol{\psi}) \equiv \int\left[\frac{\delta\mu(\mathbf{r},[\rho])}{\delta\rho(\mathbf{r}')} - \frac{\delta\mu(\mathbf{r}',[\rho])}{\delta\rho(\mathbf{r})}\right]\boldsymbol{\phi}(\mathbf{r}')\boldsymbol{\psi}(\mathbf{r})d\mathbf{r}d\mathbf{r}'. \tag{28}$$

Equation (28) is the definition of the linear operator $\mathbb{d}$ for one-forms. As in finite dimension, the exterior derivative of zero-form, i.e., a functional $\mathcal{F}[\rho]$, is then simply defined as its differential $\mathbb{d}\mathcal{F}\equiv\delta\mathcal{F}$, where $\delta\mathcal{F}$ is given by Eq. (20). Using Eqs. (20) and (28) together with the functional version of Schwarz theorem [57,58], one then checks that as expected,

$$\mathbb{d}^2 = 0, \tag{29}$$

i.e., differentials of functionals have vanishing exterior derivatives. This is the analog of gradient in three dimensions having vanishing curl. Since the functional space $\mathbb{F}$ is simply connected (being an affine space), the converse also holds, i.e., any one-form with vanishing exterior derivative is the differential of a functional. One could keep constructing exterior derivatives of higher-order forms, hence building the de Rham co-chain complex of $\mathbb{F}$, but this goes beyond the scope of this study.

5. Vorticity of AMB

Using the definition (11) of the functional vector field $\boldsymbol{\mu}$ associated to a chemical potential μ, dynamics (9) can be rewritten as

$$\partial_t\rho = -\boldsymbol{\mu} + \nabla\cdot[\sqrt{2D}\boldsymbol{\Lambda}]. \tag{30}$$

Hence, as can be seen by comparing with the finite-dimensional setting presented in Sec. II, the local vortex structure induced by the deterministic drift of dynamics (9) must be characterized by a functional vorticity two-form,

$$\boldsymbol{\omega} \equiv \mathbb{d}(-\boldsymbol{\mu})^\flat = -\mathbb{d}\boldsymbol{\mu}^\flat, \tag{31}$$

with this last equality stemming from the linearity of $\mathbb{d}$ and $\flat$. This functional vorticity (31) is—up to a factor D^{-1}—the field-theoretic analog of the cycle affinity of Markov chains. As such, it plays a similar role in the characterization of the time-reversal symmetry breaking of dynamics (9), as described in detail in the following Sec. III A 6.

Let us now compute the functional exterior derivative associated to the chemical potential μ of AMB (10). In order to lighten the notations, we will use the shorthand $f_{\mathbf{r}}$ to denote any function $f(\mathbf{r},[\rho])$. The functional derivative of μ reads

$$\frac{\delta\mu_{\mathbf{r}}}{\delta\rho_{\mathbf{r}'}} = \left[a + 3b\rho_{\mathbf{r}}^2 + \lambda_{\mathbf{r}}'|\nabla\rho_{\mathbf{r}}|^2 - \kappa_{\mathbf{r}}'\Delta\rho_{\mathbf{r}}\right]\delta(\mathbf{r}-\mathbf{r}') + 2\lambda_{\mathbf{r}}\nabla\rho_{\mathbf{r}}\cdot\nabla_{\mathbf{r}}\delta(\mathbf{r}-\mathbf{r}') - \kappa_{\mathbf{r}}\Delta_{\mathbf{r}}\delta(\mathbf{r}-\mathbf{r}'), \tag{32}$$

where $\lambda' \equiv \frac{d\lambda}{d\rho}$ and $\kappa' \equiv \frac{d\kappa}{d\rho}$. Now since $\nabla_{\mathbf{r}}\delta(\mathbf{r}-\mathbf{r}') = -\nabla_{\mathbf{r}'}\delta(\mathbf{r}-\mathbf{r}')$, Eq. (32) can be rewritten as

$$\frac{\delta\mu_{\mathbf{r}}}{\delta\rho_{\mathbf{r}'}} = \left[a + 3b\rho_{\mathbf{r}}^2 + \lambda_{\mathbf{r}}'|\nabla\rho_{\mathbf{r}}|^2 - \kappa_{\mathbf{r}}'\Delta\rho_{\mathbf{r}}\right]\delta(\mathbf{r}-\mathbf{r}') - 2\lambda_{\mathbf{r}}\nabla\rho_{\mathbf{r}}\cdot\nabla_{\mathbf{r}'}\delta(\mathbf{r}-\mathbf{r}') - \kappa_{\mathbf{r}}\Delta_{\mathbf{r}'}\delta(\mathbf{r}-\mathbf{r}'). \tag{33}$$

Using the fact that $\boldsymbol{\psi}_{\mathbf{r}}\Delta\boldsymbol{\phi}_{\mathbf{r}} - \boldsymbol{\phi}_{\mathbf{r}}\Delta\boldsymbol{\psi}_{\mathbf{r}} = \nabla\cdot(\boldsymbol{\psi}_{\mathbf{r}}\nabla\boldsymbol{\phi}_{\mathbf{r}} - \boldsymbol{\phi}_{\mathbf{r}}\nabla\boldsymbol{\psi}_{\mathbf{r}})$ and reinjecting (33) in (28), we get, after some integrations by parts,

$$\mathbb{d}\boldsymbol{\mu}^\flat(\boldsymbol{\phi},\boldsymbol{\psi}) = \int(2\lambda_{\mathbf{r}} + \kappa_{\mathbf{r}}')\nabla\rho_{\mathbf{r}}\cdot(\boldsymbol{\psi}_{\mathbf{r}}\nabla\boldsymbol{\phi}_{\mathbf{r}} - \boldsymbol{\phi}_{\mathbf{r}}\nabla\boldsymbol{\psi}_{\mathbf{r}})d\mathbf{r}. \tag{34}$$

In order to interpret Eq. (34) in a similar way to what we did for the finite-dimensional exterior derivative (8), we define the wedge product $\delta_{\mathbf{r}}\wedge\nabla\delta_{\mathbf{r}}$ between $\delta_{\mathbf{r}}$ (the Dirac at $\mathbf{r}$) and its gradient $\nabla\delta_{\mathbf{r}}$ through its action on a pair of functions

$f(\mathbf{r})$, $g(\mathbf{r})$ as

$$[\delta_{\mathbf{r}} \wedge \boldsymbol{\nabla}\delta_{\mathbf{r}}](f,g) \equiv \delta_{\mathbf{r}}(f)\boldsymbol{\nabla}\delta_{\mathbf{r}}(g) - \delta_{\mathbf{r}}(g)\boldsymbol{\nabla}\delta_{\mathbf{r}}(f) = -f_{\mathbf{r}}\boldsymbol{\nabla}g_{\mathbf{r}} + g_{\mathbf{r}}\boldsymbol{\nabla}f_{\mathbf{r}}. \tag{35}$$

We can now rewrite Eq. (34) as

$$\mathbb{d}\boldsymbol{\mu}^\flat(\boldsymbol{\phi},\boldsymbol{\psi}) = \int d\mathbf{r}\,(2\lambda_{\mathbf{r}} + \kappa'_{\mathbf{r}})\boldsymbol{\nabla}\rho_{\mathbf{r}} \cdot [\delta_{\mathbf{r}} \wedge \boldsymbol{\nabla}\delta_{\mathbf{r}}](\boldsymbol{\phi},\boldsymbol{\psi}). \tag{36}$$

The vorticity of AMB is thus given by

$$\boldsymbol{\omega} = -\mathbb{d}\boldsymbol{\mu}^\flat = -\int d\mathbf{r}\,(2\lambda + \kappa')\boldsymbol{\nabla}\rho \cdot \delta_{\mathbf{r}} \wedge \boldsymbol{\nabla}\delta_{\mathbf{r}}. \tag{37}$$

As in finite dimension (4), the vorticity $\boldsymbol{\omega}$ of the deterministic drift of Eq. (9) is also that of the (functional) velocity field $\mathbf{v}_s \equiv \mathbf{J}_s/P_s$. Indeed,

$$\mathbf{v}_s = -\boldsymbol{\mu} - D\mathbf{grad}\ln P_s, \tag{38}$$

so that its associated one-form reads

$$\mathbf{v}_s^\flat = -\boldsymbol{\mu}^\flat - D\mathbb{d}\ln P_s. \tag{39}$$

Equation (29) then allows one to conclude that

$$\boldsymbol{\omega} = \mathbb{d}\mathbf{v}_s^\flat. \tag{40}$$

In the next section, we focus on the physical content of the functional vorticity $\boldsymbol{\omega}$ of AMB, given by Eq. (37). Before we do so, let us stress that $\boldsymbol{\omega}$ measures the vortex structure of the *probability current* $\mathbf{J}_s = P_s\mathbf{v}_s$—which is a vector field over the functional space $\mathbb{F}$—and not that of any current in the real space. As such, it is not (at least directly) related to the fluid-mechanical vorticity that has been studied previously in active systems [59–61].

6. Physical interpretation and consequences

First, as discussed in Sec. III A 4, $\boldsymbol{\omega} = 0$ corresponds to the Schwarz condition under which μ is the functional derivative of a free energy [57,58]. For AMB, this reads $2\lambda + \kappa' = 0$ [49,62], which is the condition for dynamics (9) to be reversible.

Then, comparing Eq. (37) to Eq. (8), the discrete sum over $dx_i \wedge dx_j$ has been replaced by an integral over $\delta_{\mathbf{r}} \wedge \boldsymbol{\nabla}\delta_{\mathbf{r}}$. Equation (37) can thus be interpreted as follows: the flow lines of $-\boldsymbol{\mu}$ swirl around a given point ρ in $\mathbb{F}$ as soon as $(2\lambda + \kappa')\boldsymbol{\nabla}\rho \neq 0$. As in the finite-dimensional setting, such a local swirl corresponds to an infinitesimal rotation that can be decomposed into the superposition of rotations occurring in the spaces $[\rho(\mathbf{r}), \partial_x\rho(\mathbf{r}), \partial_y\rho(\mathbf{r})]$ wherever $(2\lambda + \kappa')\boldsymbol{\nabla}\rho(\mathbf{r}) \neq 0$. All in all, the flow lines of the deterministic drift tend to rotate in the 2D plane $[\rho(\mathbf{r}), \partial_k\rho(\mathbf{r})]$:

$$\begin{cases} \text{counterclockwise} & \text{iff} \quad [2\lambda + \kappa']\partial_k\rho(\mathbf{r}) > 0, \\ \text{clockwise} & \text{iff} \quad [2\lambda + \kappa']\partial_k\rho(\mathbf{r}) < 0, \end{cases} \tag{41}$$

at a speed given by the amplitude of $(2\lambda + \kappa')\partial_k\rho(\mathbf{r})$.

Let us now show that these predictions allow measurement of the steady-state currents of a phase-separated AMB. We denote by $\rho_s(\mathbf{r}) \equiv \langle\rho(\mathbf{r})\rangle$ the stationary average profile of the fluctuating field ρ. We then measure the probability current in the plane $[\rho(\mathbf{r}), \partial_x\rho(\mathbf{r})]$ at three different positions (points A, B, and C; see Fig. 1) along the horizontal diameter of the liquid droplet (see Appendix B for details about the sampling procedure). As predicted, changing the sign of $2\lambda + \kappa'$ (top vs bottom row of Fig. 1) or that of $\partial_x\rho$ (column *A* vs *C*) changes the direction of the circulation. Furthermore, the probability current vanishes in the equilibrium case $2\lambda + \kappa' = 0$ (center row), as expected.

Note that at the interface, $\rho(\mathbf{r}) \simeq \rho_s(\mathbf{r})$ and $\boldsymbol{\nabla}\rho(\mathbf{r}) \simeq \boldsymbol{\nabla}\rho_s(\mathbf{r})$, so that $\mathbb{d}\boldsymbol{\mu}^\flat|_\rho \simeq \mathbb{d}\boldsymbol{\mu}^\flat|_{\rho_s}$, which corresponds to uniform rotations in each space $[\rho(\mathbf{r}), \boldsymbol{\nabla}\rho(\mathbf{r})]$. The latter give rise to the leading-order terms of the current in the noise amplitude (columns *A* and *C*). On the contrary, in the bulk, $\boldsymbol{\nabla}\rho(\mathbf{r}) \simeq \boldsymbol{\nabla}\delta\rho(\mathbf{r})$, where $\delta\rho \equiv \rho - \rho_s$. This leads to weaker, higher order currents (column *B*).

It is tempting to split the chemical potential into $\mu = \mu_{\text{eq}} + \mu_{\text{act}}$, where μ_{eq} is the functional derivative of a free energy $\mathcal{F}$, whereas μ_{act} is not integrable, so as to identify μ_{act} as the source of irreversibility. Unfortunately, such a decomposition is not unique since adding a functional derivative $\delta\mathcal{G}/\delta\rho$ to μ_{eq} and subtracting it from μ_{act} yields another equivalent decomposition. On the contrary, $\mathbb{d}\boldsymbol{\mu}^\flat$ can *unambiguously* be identified as the source of irreversibility since the set of functional derivatives exactly coincides with the kernel of $\mathbb{d}$, so that

$$\mathbb{d}\boldsymbol{\mu}^\flat = \mathbb{d}\boldsymbol{\mu}_{\text{act}}^\flat = \mathbb{d}\big(\boldsymbol{\mu}_{\text{act}}^\flat + \mathbb{d}\mathcal{G}\big). \tag{42}$$

Propagating modes. Let us now show how our formalism yields a valuable insight into the dynamics of fluctuations. In Figs. 2(a)–2(c), we show the short-time relaxations of a perturbation $\delta\rho = \varepsilon\cos(qx)$ around a phase-separated profile ρ_s for $2\lambda + \kappa'$ negative, null, or positive. To best compare the three cases, we use the same ρ_s, corresponding to a stationary droplet for $2\lambda + \kappa' = 0$ [see Fig. 2(d)]. The analysis, detailed in Fig. 3, of the current constructed in Fig. 1 predicts that the perturbation propagates at the interface, from the liquid to the gas, when $2\lambda + \kappa' < 0$, and vice versa when $2\lambda + \kappa' > 0$. In the equilibrium case, on the contrary, the perturbation is predicted to relax to $\delta\rho = 0$ while remaining stationary. These predictions are confirmed by the simulations shown in Figs. 2(a)–2(c).

Figure 2 shows the advection of initial perturbations by the deterministic drift. In the presence of a finite noise, superpositions of the corresponding propagating modes will be constantly excited. Hence, to leading order in the noise, density fluctuations propagate radially at the interface, outwards or inwards, depending on the sign of $2\lambda + \kappa'$. This is the main real-space manifestation of the steady-state probability current. It suggests a natural mechanism to account for the continuous expulsion of bubbles, from the bubbly liquid to the gas phase, observed in the Active Model B + [63]. We note that higher-order contributions will also include orthoradial fluctuations. The latter are particularly interesting since their dynamics could offer insight into surface tension effects or capillary waves, which have recently attracted a lot of interest [64–72].

B. The Kardar-Parisi-Zhang equation

Consider the celebrated KPZ equation [26],

$$\partial_t h = -\mu + \sqrt{2D}\Lambda, \quad \mu(\mathbf{r}, [h]) = \lambda|\nabla h|^2 - \kappa\Delta h. \tag{43}$$

Here, one can conduct an analysis similar to the one we carried out for AMB in the previous sections. This would lead to directly identify $-\mu$ as a vector field on $\mathbb{F}$ (no conservation constraint over the field h) and the usual L^2–scalar product as being the appropriate Riemannian metric to construct the functional vorticity,

$$g_h(\mu_1, \mu_2) = \int \mu_1(\mathbf{r}, [h])\mu_2(\mathbf{r}, [h])d\mathbf{r}. \tag{44}$$

In this geometry, the one-form $\mu^\flat(\cdot) \equiv g(\mu, \cdot)$ associated to a vector field $\mu(\mathbf{r}, [h])$ again corresponds to integration against μ, and the vorticity of the deterministic drift of Eq. (43) is again $\boldsymbol{\omega} = -\mathbb{d}\mu^\flat$, where $\mathbb{d}\mu^\flat = \int d\mathbf{r}(2\lambda + \kappa')\nabla h \cdot \delta_\mathbf{r} \wedge \nabla\delta_\mathbf{r}$. The above analysis of the vorticity of AMB can then be directly transposed to KPZ. We thus predict that fluctuations around a height profile h should again propagates upward or downward ∇h, depending on the sign of $2\lambda + \kappa'$. These predictions are confirmed by the simulations shown in Fig. 4.

We stress that the KPZ equation and AMB describe fundamentally different physics: the unbounded growth of a fluctuating interface and the nonequilibrium phase separation of a conserved field leading to a well-defined stationary profile. These distinct long-term behaviors stem from the different irrotational component of their deterministic drifts. Importantly, our analysis reveals that, on the contrary, these systems share the same vorticity. In turn, this leads to an unexpected similarity in the dynamics of fluctuations, as seen by comparing Figs. 2 and 4.

IV. CONCLUSION

For a continuous Markov process that possesses a steady state, the curl part (in the appropriate geometry) of the deterministic drift is entirely responsible for the breakdown of detailed balance. In this article, we introduced a functional version of the curl operator: the functional exterior derivative $\mathbb{d}$, that in turn allows defining a functional vorticity, or cycle affinity. The latter offers a systematic, local, and unambiguous criterion to characterize the departure from equilibrium of spatially extended systems. It accounts for, on the one hand, the vortex structure of the stationary probability current in the space of fields and, on the other hand, the real-space manifestation of time-reversal symmetry (TRS) breaking, both of which may be quite subtle to measure.

We put this methodology at work on the Active Model B. It first allowed us to measure the appropriate 2D projections of the stationary probability current. Note that the difficulty here resides in the fact that the corresponding space is infinite dimensional, hence forbidding any attempt of brute-force sampling. In turn, we were able to unveil the real-space counterpart of these probability currents, which is the leading-order manifestation of TRS breaking in physical space, namely, the permanent excitation of anisotropic propagating modes localized at the liquid-gas interface. Since AMB was originally formulated to account for the leading-order physics of active phase separation, we expect the presence of these localized anisotropic modes to be the main qualitative difference between generic active and passive phase-separated systems, at the coarse-grained level. The fact that it remained unnoticed for such a long time, despite the extensive literature dedicated to the subject over the last 15 years, is certainly due to its localization in a noisy, relatively narrow region of space, namely, the interface between liquid and gaseous phases. This is a second difficulty which the theoretical framework presented in this article allowed one to overcome.

We also applied this formalism to the celebrated KPZ equation. As discussed in Sec. III B, despite the lack of a steady state in this process due to the irrotational part of its deterministic drift, the functional exterior derivative showed the KPZ and AMB drifts to share (for two different geometries) the same rotational part. For the KPZ equation, it is responsible for the propagation of perturbations either downward or upward the gradient of the background mean profile, depending on the parameters.

While we have focused here on the AMB and the KPZ equation, both for the sake of clarity and due to the interest they have attracted over the years, we note that our theoretical framework can be generalized to any overdamped fluctuating hydrodynamics with Gaussian noise. Suppose, for instance, that the chemical potential of Eq. (9) or (43) is given by a fourth-order expansion in gradient of ρ, i.e., $\mu = \mu_0 + \lambda|\nabla\rho|^2 - \kappa\Delta\rho + \alpha_1\Delta^2\rho + \alpha_2|\nabla\rho|^4 + \alpha_3|\nabla\rho|^2\Delta\rho + \alpha_4(\Delta\rho)^2 + \alpha_5\nabla\rho\cdot\nabla\Delta\rho$, where μ_0 is a local function of ρ and where, for the sake of clarity, all the other coefficients are taken to be constant. This situation leads to $\mathbb{d}\mu^\flat = \int d\mathbf{r}([2\lambda\nabla\rho + 4\alpha_2|\nabla\rho|^2\nabla\rho + (\alpha_5 - 2\alpha_4)\nabla\Delta\rho]\cdot\delta_\mathbf{r}\wedge\nabla\delta_\mathbf{r} + \alpha_5\nabla\rho\cdot\delta_\mathbf{r}\wedge\nabla\Delta\delta_\mathbf{r})$. Our framework thus predicts the probability currents to be localized in the spaces $[\rho(\mathbf{r}), \nabla\rho(\mathbf{r})]$ and $[\rho(\mathbf{r}), \nabla\Delta\rho(\mathbf{r})]$. More broadly, generalizing our framework to nonlocal interactions, vector or tensor fields, as well as for active mixtures [73–75], is an exciting program for the future.

ACKNOWLEDGMENTS

The author thanks Yariv Kafri, Julien Tailleur, and Frédéric van Wijland for useful comments on the manuscript.

APPENDIX A: SIMULATING AMB DYNAMICS

The numerical simulations of the dynamics of AMB were realized through the discretization of the field on a lattice of $N_x \times N_y$ sites, with periodic boundary conditions and a discretization step dx (dy) in the x direction (in the y direction),

$$\rho_t(x, y) \longrightarrow \rho_{n_t}(n_x, n_y) \equiv \rho_{n_t dt}(n_x dx, n_y dy), \tag{A1}$$

where $(n_x, n_y) \in [\![0, N_x - 1]\!] \times [\![0, N_y - 1]\!]$. We used the discrete gradient given by

$$\nabla\rho(i, j) \equiv \left(\frac{\rho(i+1, j) - \rho(i-1, j)}{2dx}, \frac{\rho(i, j+1) - \rho(i, j-1)}{2dy}\right) \tag{A2}$$

and the discrete Laplacian

$$\Delta\rho(i,j) = \frac{\rho(i+1,j)+\rho(i-1,j)-2\rho(i,j)}{dx^2} + \frac{\rho(i,j+1)+\rho(i,j-1)-2\rho(i,j)}{dy^2}. \quad \text{(A3)}$$

In the simulations, we considered λ and κ constants. In addition, in order to stabilize the simulations, we used an implicit time-discretization scheme for the term proportional to κ in the dynamics of AMB. Hence, our discrete version of Eq. (9) reads

$$\frac{\rho_{n_t+1}-\rho_{n_t}}{dt} = -\kappa\Delta^2\rho_{n_t+1} + \Delta\left[a\rho_{n_t} + b\rho_{n_t}^3 + \lambda|\nabla\rho_{n_t}|^2\right] + \boldsymbol{\nabla}\cdot\boldsymbol{\Lambda}_{n_t}, \quad \text{(A4)}$$

where we omitted the spatial discrete variable (n_x, n_y) for the sake of clarity. At time n_t, each component of the noise $\boldsymbol{\Lambda}_{n_t}$ is a random Gaussian variable of zero average and variance $\frac{2D}{dxdydt}$.

Note that the discrete field $\rho(n_x, n_y)$ can alternatively be described through its discrete Fourier transform (DFT),

$$\hat{\rho}(k_x.k_y) \equiv \sum_{n_x=0}^{N_x-1}\sum_{n_y=0}^{N_y-1}\rho(n_x,n_y)e^{-2i\pi\left(\frac{k_x n_x}{N_x}+\frac{k_y n_y}{N_y}\right)}. \quad \text{(A5)}$$

The inverse DFT of $\hat{\rho}(k_x, k_y)$ gives back the initial field,

$$\rho(n_x,n_y) = \frac{1}{N_x N_y}\sum_{k_x=0}^{N_x-1}\sum_{k_y=0}^{N_y-1}\hat{\rho}(k_x,k_y)e^{2i\pi\left(\frac{k_x n_x}{N_x}+\frac{k_y n_y}{N_y}\right)}. \quad \text{(A6)}$$

The discrete Fourier transform (DFT) of the discrete gradient (A2) is thus

$$\hat{\nabla} = \left(\frac{i}{dx}\sin\left[\frac{2\pi k_x}{N_x}\right], \frac{i}{dy}\sin\left[\frac{2\pi k_y}{N_y}\right]\right), \quad \text{(A7)}$$

while the DFT of the discrete Laplacian (A3) is given by

$$\hat{\Delta} = -4\left[\frac{1}{dx^2}\sin^2\left(\frac{\pi k_x}{N_x}\right) + \frac{1}{dy^2}\sin^2\left(\frac{\pi k_y}{N_y}\right)\right]. \quad \text{(A8)}$$

Note that computing ρ_{n_t+1} from ρ_{n_t} via Eq. (A4) requires the inversion of the operator $(1+\kappa dt\Delta^2)$. The latter being linear and invariant by translation, it is diagonal in the Fourier basis. Hence, to make things easier, we compute the inverse of this operator in the Fourier basis.

All in all, knowing the state of the field ρ_{n_t} and of its DFT $\hat{\rho}_{n_t}$ at a given time step n_t, we compute ρ_{n_t+1} through the following algorithm:

(i) We compute the nonlinear terms $f_{n_t}(n_x,n_y) \equiv a\rho_{n_t}(n_x,n_y) + b\rho_{n_t}^3(n_x,n_y) + \lambda|\nabla\rho_{n_t}(n_x,n_y)|^2$ in direct space.

(ii) We draw all the noise terms $\boldsymbol{\Lambda}_{n_t}(n_x,n_y)$ independently from $\mathcal{N}(0, 2D/[dxdydt])$.

(iii) We compute the DFTs $\hat{f}_{n_t}$ and $\hat{\boldsymbol{\Lambda}}_{n_t}$.

(iv) We compute $\hat{\rho}_{n_t+1}$ through

$$\hat{\rho}_{n_t+1} = [1+\kappa dt\hat{\Delta}^2]^{-1}[\hat{\rho}_{n_t} + dt\hat{\Delta}f_{n_t} + dt\hat{\nabla}\cdot\hat{\boldsymbol{\Lambda}}_{n_t}]. \quad \text{(A9)}$$

Figures 1 and 2 of the main text have been generated using the semispectral numerical integration of the AMB dynamics described above, with $N_x = N_y = 256$, $dx = dy = 10/256$, and a time step $dt = 10^{-6}$. The other parameters are given in the caption of each figure.

APPENDIX B: SAMPLING (PROJECTIONS OF) THE STATIONARY PROBABILITY CURRENT

The projected probability current $\pi_{\mathbf{r}_0}[\mathbf{J}_s]$ in the space $[\rho(\mathbf{r}_0), \partial_k\rho(\mathbf{r}_0)]$ at a given point $\mathbf{r}_0$ is the vector field whose value at a point $[\rho(\mathbf{r}_0), \partial_k\rho(\mathbf{r}_0)]$ is given by

$$\pi_{\mathbf{r}_0}[\mathbf{J}_s] = \langle[\dot{\rho}_t(\mathbf{r}_0), \partial_k\dot{\rho}_t(\mathbf{r}_0)]\delta[\rho_t(\mathbf{r}_0)-\rho(\mathbf{r}_0)] \times \delta[\partial_k\rho_t(\mathbf{r}_0)-\partial_k\rho(\mathbf{r}_0)]\rangle, \quad \text{(B1)}$$

where the time derivatives are defined in the Stratonovich sense, and $\langle\cdot\rangle$ denotes the average in the steady state (conditioned to a fixed droplet center). Given the ergodicity of dynamics (9), the current (B1) is also given by the time average,

$$\pi_{\mathbf{r}_0}[\mathbf{J}_s] = \lim_{T\to\infty}\frac{1}{T}\int_0^T [\dot{\rho}_t(\mathbf{r}_0), \partial_k\dot{\rho}_t(\mathbf{r}_0)]\delta[\rho_t(\mathbf{r}_0)-\rho(\mathbf{r}_0)] \times \delta[\partial_k\rho_t(\mathbf{r}_0)-\partial_k\rho(\mathbf{r}_0)]dt, \quad \text{(B2)}$$

where the stochastic integral is defined in the Stratonovich sense. Figure 1 of the main text was realized by sampling $\pi_{\mathbf{r}_0}[\mathbf{J}_s]$ at different points $\mathbf{r}_0$.

APPENDIX C: SIMULATING THE KPZ EQUATION

The numerical simulations of the KPZ equation were realized on a one-dimensional lattice, with fixed Dirichlet boundary conditions. We used the same space discretization of the ∇ and Δ operators as in Appendix A. We used a fully explicit time-discretization scheme, and computed the value of h_{n_t+1} from that h_{n_t} in direct space.

[1] J. L. Lebowitz and H. Spohn, J. Stat. Phys. **95**, 333 (1999).
[2] J. Kurchan, J. Phys. A: Math. Gen. **31**, 3719 (1998).
[3] C. Maes, J. Stat. Phys. **95**, 367 (1999).
[4] T. Hatano and S.-i. Sasa, Phys. Rev. Lett. **86**, 3463 (2001).
[5] U. Seifert, Phys. Rev. Lett. **95**, 040602 (2005).
[6] L. F. Cugliandolo, J. Phys. A: Math. Theor. **44**, 483001 (2011).
[7] A. Pérez-Madrid, D. Reguera, and J. Rubı, Physica A **329**, 357 (2003).
[8] R. P. Feynman, R. B. Leighton, and M. Sands, *The Feynman Lectures on Physics, Vol. I: The New Millennium Edition: Mainly Mechanics, Radiation, and Heat* (Basic Books, New York, 2011), Vol. 1.
[9] J. M. Parrondo and P. Español, Am. J. Phys. **64**, 1125 (1996).
[10] P. Hänggi and F. Marchesoni, Rev. Mod. Phys. **81**, 387 (2009).
[11] M. O. Magnasco, Phys. Rev. Lett. **71**, 1477 (1993).
[12] R. Zia and B. Schmittmann, J. Stat. Mech.: Theory Expt. (2007) P07012.
[13] R. Zia and B. Schmittmann, Phys. Proc. **7**, 112 (2010).
[14] T. B. Liverpool, Phys. Rev. E **101**, 042107 (2020).
[15] L. Bertini, A. De Sole, D. Gabrielli, G. Jona-Lasinio, and C. Landim, Rev. Mod. Phys. **87**, 593 (2015).

[16] B. Schmittmann and R. K. Zia, Phase Transitions Crit. Phenom. **17**, 3 (1995).
[17] G. L. Eyink, J. L. Lebowitz, and H. Spohn, J. Stat. Phys. **83**, 385 (1996).
[18] B. Derrida, J. Lebowitz, and E. Speer, J. Stat. Phys. **107**, 599 (2002).
[19] T. Bodineau and B. Derrida, Phys. Rev. Lett. **92**, 180601 (2004).
[20] J. Tailleur and M. E. Cates, Phys. Rev. Lett. **100**, 218103 (2008).
[21] C. Nardini, É. Fodor, E. Tjhung, F. van Wijland, J. Tailleur, and M. E. Cates, Phys. Rev. X **7**, 021007 (2017).
[22] É. Fodor, C. Nardini, M. E. Cates, J. Tailleur, P. Visco, and F. van Wijland, Phys. Rev. Lett. **117**, 038103 (2016).
[23] J. O'Byrne, Y. Kafri, J. Tailleur, and F. van Wijland, Nat. Rev. Phys. **4**, 167 (2022).
[24] P. Galajda, J. Keymer, P. Chaikin, and R. Austin, J. Bacteriol. **189**, 8704 (2007).
[25] E. Flenner and G. Szamel, Phys. Rev. E **102**, 022607 (2020).
[26] M. Kardar, G. Parisi, and Y.-C. Zhang, Phys. Rev. Lett. **56**, 889 (1986).
[27] H. Hinrichsen, Adv. Phys. **49**, 815 (2000).
[28] M. Baiesi and C. Maes, New J. Phys. **15**, 013004 (2013).
[29] S. Dal Cengio, D. Levis, and I. Pagonabarraga, J. Stat. Mech.: Theory Expt. (2021) 043201.
[30] H. Ge, Phys. Rev. E **89**, 022127 (2014).
[31] M. Baiesi, E. Boksenbojm, C. Maes, and B. Wynants, J. Stat. Phys. **139**, 492 (2010).
[32] N. Freitas, J.-C. Delvenne, and M. Esposito, Phys. Rev. X **10**, 031005 (2020).
[33] J. Kurchan, arXiv:0901.1271.
[34] M. Kaiser, R. L. Jack, and J. Zimmer, J. Stat. Phys. **170**, 1019 (2018).
[35] X. Fang, K. Kruse, T. Lu, and J. Wang, Rev. Mod. Phys. **91**, 045004 (2019).
[36] H. Feng and J. Wang, J. Chem. Phys. **135**, 234511 (2011).
[37] J. Wang, Adv. Phys. **64**, 1 (2015).
[38] M. Polettini, Europhys. Lett. **97**, 30003 (2012).
[39] U. C. Täuber, *Critical Dynamics: A Field Theory Approach to Equilibrium and Non-equilibrium Scaling Behavior* (Cambridge University Press, Cambridge, 2014).
[40] M. Kardar, *Statistical Physics of Fields* (Cambridge University Press, Cambridge, 2007).
[41] J. Cardy, *Scaling and Renormalization in Statistical Physics*, Vol. 5 (Cambridge University Press, Cambridge, 1996).
[42] Ø. L. Borthne, É. Fodor, and M. E. Cates, New J. Phys. **22**, 123012 (2020).
[43] F. Caballero and M. E. Cates, Phys. Rev. Lett. **124**, 240604 (2020).
[44] Y. I. Li and M. E. Cates, J. Stat. Mech.: Theory Expt. (2021) 013211.
[45] J. Gladrow, N. Fakhri, F. C. MacKintosh, C. F. Schmidt, and C. P. Broedersz, Phys. Rev. Lett. **116**, 248301 (2016).
[46] C. Battle, C. P. Broedersz, N. Fakhri, V. F. Geyer, J. Howard, C. F. Schmidt, and F. C. MacKintosh, Science **352**, 604 (2016).
[47] I. M. Anderson, The variational bicomplex, Technical Report (Utah State Technical Report, 1989), https://ncatlab.org/nlab/files/AndersonVariationalBicomplex.pdf.
[48] A. Kriegl and P. W. Michor, *The Convenient Setting of Global Analysis* (American Mathematical Society, Providence, RI, 1997), Vol. 53.
[49] R. Wittkowski, A. Tiribocchi, J. Stenhammar, R. J. Allen, D. Marenduzzo, and M. E. Cates, Nat. Commun. **5**, 4351 (2014).
[50] D. Martin, J. O'Byrne, M. Cates, É. Fodor, C. Nardini, J. Tailleur, and F. van Wijland, Phys. Rev. E **103**, 032607 (2021).
[51] Y.-J. Yang and H. Qian, J. Stat. Phys. **182**, 46 (2021).
[52] T. L. Hill, *Free Energy Transduction and Biochemical Cycle Kinetics* (Springer, New York, 1989).
[53] J. Schnakenberg, Rev. Mod. Phys. **48**, 571 (1976).
[54] D.-Q. Jiang and D. Jiang, *Mathematical Theory of Nonequilibrium Steady States: On the Frontier of Probability and Dynamical Systems* (Springer Science & Business Media, Berlin, 2004).
[55] D. S. Dean, J. Phys. A: Math. Gen. **29**, L613 (1996).
[56] F. Otto, Communic. Part. Different. Equat. **26**, 101 (2001).
[57] J. O'Byrne and J. Tailleur, Phys. Rev. Lett. **125**, 208003 (2020).
[58] T. Grafke, M. E. Cates, and E. Vanden-Eijnden, Phys. Rev. Lett. **119**, 188003 (2017).
[59] A. Doostmohammadi, M. F. Adamer, S. P. Thampi, and J. M. Yeomans, Nat. Commun. **7**, 10557 (2016).
[60] A. Souslov, K. Dasbiswas, M. Fruchart, S. Vaikuntanathan, and V. Vitelli, Phys. Rev. Lett. **122**, 128001 (2019).
[61] D. Banerjee, A. Souslov, A. G. Abanov, and V. Vitelli, Nat. Commun. **8**, 1573 (2017).
[62] A. P. Solon, J. Stenhammar, M. E. Cates, Y. Kafri, and J. Tailleur, Phys. Rev. E **97**, 020602(R) (2018).
[63] E. Tjhung, C. Nardini, and M. E. Cates, Phys. Rev. X **8**, 031080 (2018).
[64] J. Bialké, J. T. Siebert, H. Löwen, and T. Speck, Phys. Rev. Lett. **115**, 098301 (2015).
[65] U. M. B. Marconi, C. Maggi, and S. Melchionna, Soft Matter **12**, 5727 (2016).
[66] S. Paliwal, V. Prymidis, L. Filion, and M. Dijkstra, J. Chem. Phys. **147**, 084902 (2017).
[67] A. Patch, D. M. Sussman, D. Yllanes, and M. C. Marchetti, Soft Matter **14**, 7435 (2018).
[68] R. Wittmann, F. Smallenburg, and J. M. Brader, J. Chem. Phys. **150**, 174908 (2019).
[69] R. Zakine, Y. Zhao, M. Knežević, A. Daerr, Y. Kafri, J. Tailleur, and F. van Wijland, Phys. Rev. Lett. **124**, 248003 (2020).
[70] A. Wysocki and H. Rieger, Phys. Rev. Lett. **124**, 048001 (2020).
[71] A. K. Omar, Z.-G. Wang, and J. F. Brady, Phys. Rev. E **101**, 012604 (2020).
[72] N. Lauersdorf, T. Kolb, M. Moradi, E. Nazockdast, and D. Klotsa, Soft Matter **17**, 6337 (2021).
[73] S. Saha, J. Agudo-Canalejo, and R. Golestanian, Phys. Rev. X **10**, 041009 (2020).
[74] Z. You, A. Baskaran, and M. C. Marchetti, Proc. Natl. Acad. Sci. USA **117**, 19767 (2020).
[75] A. Dinelli, J. O'Byrne, A. Curatolo, Y. Zhao, P. Sollich, and J. Tailleur, arXiv:2203.07757.